



FLEX: Low-Complexity 5D Beamspace Channel Estimation for mmWave MIMO-OFDM

Downloaded from: <https://research.chalmers.se>, 2026-05-08 14:15 UTC

Citation for the original published paper (version of record):

Pourafzal, A., Huang, H., Pettersson, V. et al (2025). FLEX: Low-Complexity 5D Beamspace Channel Estimation for mmWave MIMO-OFDM. European Signal Processing Conference. <http://dx.doi.org/10.23919/EUSIPCO63237.2025.11226647>

N.B. When citing this work, cite the original published paper.

FLEX: Low-Complexity 5D Beamspace Channel Estimation for mmWave MIMO-OFDM

Alireza Pourafzal, Huiping Huang, Victor Pettersson, Musa Furkan Keskin, and Henk Wymeersch
Department of Electrical Engineering, Chalmers University of Technology, Sweden

E-mail: alireza.pourafzal@chalmers.se

Abstract—We introduce FLEX, a family of fast Fourier transform(FFT)-based low complexity beamspace channel estimation algorithms for mmWave MIMO-OFDM systems, enabling five-dimensional parameter estimation; delay, two-dimensional angles of arrival (AoAs), and two-dimensional angles of departure (AoDs). FLEX operates without prior knowledge of the number of propagation paths and automatically pairs multidimensional parameters. The proposed methods first estimate path delays using an FFT-based approach, then compensate for these delays to decouple the spatial dimensions. Angle estimation is performed using either a correlation-based or an ESPRIT-based method, accommodating different precoder structures. A modified approach resolves paths that share a delay bin but are separable in angular domain. Simulation results demonstrate that FLEX significantly reduces computational complexity while achieving accuracy comparable to state-of-the-art methods, converging to theoretical bounds at lower transmit power. Its efficiency and adaptability make FLEX well-suited for real-time channel estimation in wideband communication systems.

Index Terms—Channel Estimation, MIMO-OFDM, hybrid array, angle-of-arrival, angle-of-departure, time-of-arrival.

I. INTRODUCTION

Millimeter-wave (mmWave) MIMO is fundamental for next-generation wireless networks, offering high data rates and massive connectivity [1]. The combination of high carrier frequencies and large-scale antenna arrays in mmWave systems offers significant beamforming gains, yet also poses challenges in channel estimation. Unlike sub-6 GHz systems, mmWave channels typically exhibit sparse multipath propagation with only a few dominant clusters [2]. To fully exploit this sparsity, accurate and efficient estimation of the high-dimensional channel parameters, such as time of arrival (ToA), angle of arrival (AoA), and angle of departure (AoD), is critical, especially for wideband systems.

Existing methods for channel estimation include subspace methods, compressed sensing, tensor decomposition, and their combinations. Subspace methods require orthogonality, suffer in low signal-to-noise ratio (SNR), and often need pairing

between estimated parameters. Compressed sensing (e.g. orthogonal matching pursuit (OMP), Bayesian recovery [2], [3]) performs well but their performance depends on grid resolution and computational costs increase with large bandwidths. Tensor decomposition methods (such as RD-BeamESPRIT [4] and CP decomposition) provide low-complexity estimates, but demands high SNR and often assume a fixed number of paths. Furthermore, existing methods either assume prior knowledge of the number of paths [2], [5], structural constraints such as beam orthogonality [3], require parameter pairing [6], or incur a high computational cost [2], [3]. These limitations highlight the need for robust, low-complexity estimation techniques.

In this paper, we propose FLEX, a family of low-complexity solutions for five-dimensional channel parameter estimation (2D AoA, 2D AoD, and delay) tailored to mmWave MIMO-OFDM. FLEX leverages the asymmetries in the resolutions in a practical mmWave setup, and extracts path delays via a discrete Fourier transform (DFT)-based approach, then isolates each path in the spatial domain. No prior knowledge of the number of paths is required. We develop two variants, one using correlation-based beam alignment and another using an estimation of signal parameters via rotational invariance techniques (ESPRIT)-based method, to utilize the orthogonality structure in the beamforming design. A further modification resolves paths with identical delays but separable angles. With numerical simulations, we evaluated FLEX against the state-of-the-art (SoTA) methods in terms of accuracy, range resolution, and computational complexity.

Notations: Matrices are bold uppercase (\mathbf{A}), vectors bold lowercase (\mathbf{a}), element indices superscripts (\mathbf{a}^i), and tensors calligraphic (\mathcal{X}). Operations include transpose (\cdot^T), conjugate (\cdot^*), conjugate transpose (\cdot^H), tensor unfolding $[\cdot]_x$, Khatri-Rao product (\star), and Kronecker product (\otimes). $\mathbf{I}_M \in \mathbb{R}^{M \times M}$ is the identity matrix, and $\mathbf{0}_M \in \mathbb{C}^{M \times 1}$ is an all-zeros vector. $\arg(\exp(j\omega)) = \omega$, and $(\cdot)^\dagger$ is the Moore–Penrose inverse.

II. SYSTEM MODEL

A. Channel Model

The base station (BS) and user equipment (UE) each have uniform rectangular array (URA) antennas with $N_{\text{BS}} = N_1 \times N_2$ and $N_{\text{UE}} = N_3 \times N_4$ elements ($N_{\text{BS}} \gg N_{\text{UE}}$). Communication occurs in the mmWave band with limited scattering [7]. In addition to the line-of-sight (LoS), $L - 1$ scattering points exist, each contributing a single propagation

This work is supported by the Vinnova B5GPOS Project under Grant 2022-01640 and the Swedish Research Council (VR) through the project 6G-PERCEF under Grant 2024-04390. The computations were enabled by resources provided by the National Academic Infrastructure for Supercomputing in Sweden (NAISS), partially funded by the Swedish Research Council through grant agreement no. 2022-06725.

Copyright notice: © 2026 IEEE. Personal use of this material is permitted. Permission from IEEE must be obtained for all other uses, including reprinting/republishing this material for advertising or promotional purposes, creating new collective works for resale or redistribution, or reuse of any copyrighted component of this work in other works.

path with a single bounce [8]. The frequency domain channel $\mathbf{H}(f) \in \mathbb{C}^{N_{\text{UE}} \times N_{\text{BS}}}$ is [9]

$$\mathbf{H}(f) = \sum_{l=0}^{L-1} \alpha_l \mathbf{a}_{\text{UE}}(\phi_l) \mathbf{a}_{\text{BS}}^T(\theta_l) e^{-j2\pi f \tau_l}, \quad (1)$$

where α_l is the complex gain of path l , and $\mathbf{a}_{\text{UE}} \in \mathbb{C}^{N_{\text{UE}}}$ and $\mathbf{a}_{\text{BS}} \in \mathbb{C}^{N_{\text{BS}}}$ are the steering vectors for the UE and BS, with spatial frequencies ϕ_l and θ_l , associated with two-dimensional AoA and AoD, respectively. They are defined as $\mathbf{a}_{\text{UE}} = \mathbf{a}_{N_3}(\omega_3^1) \otimes \mathbf{a}_{N_4}(\omega_4^1)$ and $\mathbf{a}_{\text{BS}} = \mathbf{a}_{N_1}(\omega_1^1) \otimes \mathbf{a}_{N_2}(\omega_2^1)$, where $\mathbf{a}_N(\omega) = [1, e^{j\omega}, \dots, e^{j(N-1)\omega}]$. Here, $\omega_l^{1,2} = \theta_l$ and $\omega_l^{3,4} = \phi_l$, where $\omega_l^{1,3}$ correspond to the x-axis of the antennas, and $\omega_l^{2,4}$ to the y-axis. The propagation delay is τ_l , and f denotes the working frequency.

B. Signal Model

Consider a downlink scenario where the BS transmits S orthogonal frequency division multiplexing (OFDM) blocks, each with M symbols across K subcarriers. For subcarrier k , symbol m , and block s , the received signal at the UE is

$$y_{m,s,k} = \mathbf{w}_m^H \mathbf{H}(k\Delta f) \mathbf{f}_s + q_{m,s,k}, \quad (2)$$

where $\mathbf{w}_m \in \mathbb{C}^{N_{\text{UE}} \times 1}$ and $\mathbf{f}_s \in \mathbb{C}^{N_{\text{BS}} \times 1}$ are the UE combiner and BS precoder, respectively, Δf is the subcarrier spacing, and $q_{m,s,k} \sim \mathcal{CN}(0, \sigma_q^2)$ is the noise floor. The precoder and combiner are linked to a single radio frequency chain (RFC).

Stacking (2) into a tensor $\mathcal{Y} \in \mathbb{C}^{M \times S \times K}$, where $\mathcal{Y}^{m,s,k} = y_{m,s,k}$, we express the received signal as the perturbed canonical polyadic (CP) model [10]–[12]

$$\mathcal{Y} = \mathcal{H} + \mathcal{Q}, \quad (3)$$

where $\mathcal{H} = \mathcal{C} \times_1 \mathbf{B}_1 \times_2 \mathbf{B}_2 \times_3 \mathbf{B}_3$, with $\mathcal{C} \in \mathbb{C}^{L \times L \times L}$ satisfying $\mathcal{C}^{l,l,l} = \alpha_l$ and zero elsewhere, and $\mathcal{Q}^{s,m,k} = q_{s,m,k}$. The factor matrices $\mathbf{B}_{\{1,2,3\}} \in \mathbb{C}^{\{M,S,K\} \times L}$ have columns $\mathbf{b}_{1,l} = \mathbf{W}^H \mathbf{a}_{\text{UE}}(\theta_l)$, $\mathbf{b}_{2,l} = \mathbf{F}^T \mathbf{a}_{\text{BS}}(\phi_l)$, and $\mathbf{b}_{3,l} = e^{-j2\pi \Delta f k \tau_l}$. Here, $\mathbf{W} = [\mathbf{w}_0, \dots, \mathbf{w}_{M-1}]$ and $\mathbf{F} = [\mathbf{f}_0, \dots, \mathbf{f}_{S-1}]$, are designed via codebook-based beam switching [13] and have Kronecker structures: $\mathbf{F} = \mathbf{T}_1^* \otimes \mathbf{T}_2^*$ and $\mathbf{W} = \mathbf{T}_3 \otimes \mathbf{T}_4$ [14], where $\mathbf{T}_r \in \mathbb{C}^{N_r \times M_r}$ and $M_1 M_2 = S$, $M_3 M_4 = M$.

III. PROPOSED CHANNEL ESTIMATION METHOD

We introduce a channel estimation framework that sequentially estimates the parameters of each dimension, starting with delay estimation (where the resolution is highest) and decoupling each from the observed tensor. Details follow.

A. Unfolding Operation

To estimate the channel's delay, we create the third unfolding matrix of the tensor \mathcal{Y} , expressed as $[\mathcal{Y}]_{(3)} \in \mathbb{C}^{K \times SM}$. This operation rearranges the delay-associated slice as the frontal slice. Following (3), we get

$$[\mathcal{Y}]_{(3)} = [\mathcal{H}]_{(3)} + [\mathcal{Q}]_{(3)}. \quad (4)$$

Equation (4) is valid because the unfolding operations preserve the structure of tensors of identical sizes [15], and matrix addition is commutative. Defining $\mathbf{V} = \mathbf{B}_1 \star \mathbf{B}_2 = [\mathbf{v}_0, \mathbf{v}_1, \dots, \mathbf{v}_{L-1}] \in \mathbb{C}^{SM \times L}$, $[\mathcal{H}]_{(3)}$ is modeled as [16]

$$[\mathcal{H}]_{(3)} = \mathbf{B}_3 \mathbf{\Lambda} \mathbf{V}^T = \sum_l \alpha_l \mathbf{b}_{3,l} \mathbf{v}_l^T, \quad (5)$$

where $\mathbf{\Lambda} \in \mathbb{C}^{L \times L}$ is a diagonal matrix such that $\mathbf{\Lambda}^{l,l} = \alpha_l$.

B. Delay Estimation

To simplify delay estimation from raw observed signals, we apply the DFT. The method incorporates non-coherent combining across symbols and transmissions to enhance SNR, followed by thresholding and peak detection for accurate delay estimation.

1) *DFT and Periodogram*: Let $\mathbf{y}_s \in \mathbb{C}^{K \times 1}$, where each component \mathbf{y}_s^k is defined as $\mathbf{y}_s^k = ([\mathcal{Y}]_{(3)}^{k,s})^*$ for $s \in \{0, 1, \dots, SM-1\}$. The k_{DFT} -th DFT coefficient of \mathbf{y}_s is

$$\mathbf{F}(\mathbf{y}_s, k_{\text{DFT}}) = \frac{1}{K} \sum_{k=0}^{K-1} \mathbf{y}_s^k e^{-j2\pi \frac{k_{\text{DFT}}}{K} k}, \quad (6)$$

which based on (4), is decomposed to

$$\mathbf{F}(\mathbf{y}_s, k_{\text{DFT}}) = \mathbf{F}(\mathbf{h}_s, k_{\text{DFT}}) + \mathbf{F}(\mathbf{q}_s, k_{\text{DFT}}), \quad (7)$$

where $k_{\text{DFT}} \in \{0, 1, \dots, K_{\text{DFT}}-1\}$, $\mathbf{q}_s^k = ([\mathcal{Q}]_{(3)}^{k,s})^*$ and $\mathbf{h}_s^k = ([\mathcal{H}]_{(3)}^{k,s})^*$. According to (5), \mathbf{h}_s contains the conjugate elements of the delay vector $\mathbf{b}_{3,l}$, with a DFT of

$$\mathbf{F}(\mathbf{h}_s, k_{\text{DFT}}) = \frac{1}{K} \sum_{l=0}^{L-1} (\alpha_l \mathbf{v}_l^s)^* \frac{1 - e^{j2K\Delta\omega_l}}{1 - e^{j2\Delta\omega_l}} \quad (8)$$

where $\Delta\omega_l = \pi(\Delta f \tau_l - \frac{k_{\text{DFT}}}{K_{\text{DFT}}})$. Considering \mathbf{h}_s across different s is independent of k , we treat \mathbf{h}_s as observations from multiple snapshots. The periodogram averaging of multiple snapshots based on Bartlett's method [17], is calculated as

$$\mathbf{P}(\mathbf{y}_s, k_{\text{DFT}}) = \frac{1}{SM} \sum_{s=0}^{SM-1} |\mathbf{F}(\mathbf{y}_s, k_{\text{DFT}})|^2. \quad (9)$$

2) *Thresholding and Peak Detection*: For thresholding, we utilize the cell averaging constant false alarm rate (CA-CFAR) detection mechanism [18], incorporating a threshold factor based on a desired false alarm probability p_{FA} (manual threshold). The selection of CA-CFAR is motivated by the problem of signal periodogram leakage into the sidelobes, which makes detectors with a fixed threshold suboptimal in the Neyman-Pearson sense [19]. According to the Cauchy-Schwarz inequality and (7), $\mathbf{P}(\mathbf{y}_s, k_{\text{DFT}})$ is bounded as

$$\mathbf{P}(\mathbf{y}_s, k_{\text{DFT}}) \leq \mathbf{P}(\mathbf{h}_s, k_{\text{DFT}}) + \mathbf{P}(\mathbf{q}_s, k_{\text{DFT}}). \quad (10)$$

To determine the threshold, we analyze the noise periodogram. The noise DFT output follows a complex Gaussian distribution with zero mean and variance σ_q^2/K , leading to a Gamma-distributed noise periodogram $\mathbf{P}(\mathbf{q}_s, k_{\text{DFT}}) \sim \Gamma(SM, \sigma_q^2/(SMK))$. The threshold factor ξ is derived from the inverse Gamma cumulative distribution function, $\Gamma^{-1}(\cdot)$, for a given false alarm probability p_{FA} , as

$$\xi = \Gamma^{-1}(p_{\text{FA}} | SM, \sigma_q^2/(SMK)) / (\sigma_q^2/K). \quad (11)$$

This ensures Neyman-Pearson detection under noise-only conditions while compensating for sidelobe leakage when signals are present. A neighborhood is selected if

$$\mathbf{P}(\mathbf{y}_s, k_{\text{DFT}}) \geq \xi \mathbb{E}[\mathbf{P}(\mathbf{y}_s, j)], \quad (12)$$

for all j within the training cells [18].

The next step involves identifying the peaks of the neighborhoods that exceed the threshold. Assuming $K \gg 1$, the

DFT of \mathbf{h}_s at frequency k_{DFT} in (8) is approximated by

$$F(\mathbf{h}_s, k_{\text{DFT}}) \approx \sum_{l=0}^{L-1} (\alpha_l \mathbf{v}_l^s)^* e^{j\frac{\Delta\omega l}{2}(K-1)} \text{sinc}\left(K\frac{\Delta\omega l}{\pi}\right). \quad (13)$$

Consequently, the periodogram of \mathbf{h}_s is approximated as

$$P(\mathbf{h}_s, k_{\text{DFT}}) \approx K \sum_{l=0}^{L-1} |\alpha_l|^2 \left| \text{sinc}\left(K\frac{\Delta\omega l}{\pi}\right) \right|^2, \quad (14)$$

yielding a resolution of $\Delta\omega = 2\pi/K$. We select local maxima \hat{k}_i that exceed the CA-CFAR threshold as defined in (12) and are separated by at least the resolution value $2K_{\text{DFT}}/K$ (i.e. eliminating multiple detections from a single resolution cell). Delay estimates are calculated using $\hat{\tau}_i = \hat{k}_i / (\Delta f K_{\text{DFT}})$.

C. Decoupling Observed Tensor from Delay

Let $\hat{\tau}_i \in \{\hat{\tau}_0, \hat{\tau}_1, \dots, \hat{\tau}_{L-1}\} = \{\tau_0, \tau_1, \dots, \tau_{L-1}\}^1$ where \hat{L} is the number of estimated delays. We define a matrix $\hat{\mathbf{B}}_3$, such that $\hat{\mathbf{B}}_3^{k,i} = e^{+j2\pi\Delta f k \hat{\tau}_i}$. This matrix is related to \mathbf{B}_3 through a permutation matrix $\mathbf{\Pi}$, as $\hat{\mathbf{B}}_3 = \mathbf{B}_3 \mathbf{\Pi}$. The third mode product between \mathcal{Y} and $\hat{\mathbf{B}}_3$ decouples the delay dimension as

$$\mathcal{Y}_{\text{sub}} = \mathcal{Y} \times_3 \hat{\mathbf{B}}_3^\dagger = \mathcal{H}_{\text{sub}} + \mathcal{Q}_{\text{sub}}, \quad (15)$$

where $\mathcal{H}_{\text{sub}} = \mathcal{C} \times_1 \mathbf{B}_1 \times_2 \mathbf{B}_2 \times_3 \mathbf{\Pi}$ and $\mathcal{Q}_{\text{sub}} = \mathcal{Q} \times_3 \hat{\mathbf{B}}_3^\dagger$. As $\mathbf{\Pi}$ only reorders the slices from l to i , the sub-tensor \mathcal{H}_{sub} can be represented as a concatenation of \hat{L} tensors [16]

$$\mathcal{H}_{\text{sub}} = \mathcal{H}_{\text{sub},0} \sqcup \mathcal{H}_{\text{sub},1} \sqcup \dots \sqcup \mathcal{H}_{\text{sub},\hat{L}-1}, \quad (16)$$

where $\mathcal{H}_{\text{sub},i} = \alpha_i \mathbf{b}_{1,i} \circ \mathbf{b}_{2,i}$. To decouple the delay of the i -th path, we extract the i -th slice of \mathcal{Y}_{sub} , and unfold it to the vector \mathbf{x}_i defined as $\mathbf{x}_i = [\mathcal{Y}_{\text{sub}}^{i,i}]_{(1)}$. The vector \mathbf{x}_i is modeled as $\mathbf{x}_i = \mathbf{a}_i + \mathbf{q}_i$ where $\mathbf{q}_i = [\mathcal{Q}_{\text{sub}}^{i,i}]_{(1)}$, and $\mathbf{a}_i = [\mathcal{H}_{\text{sub},i}]_{(1)}$.

D. Angle Estimation

The vector \mathbf{a}_i is expressed as $\mathbf{a}_i = \alpha_i (\mathbf{u}_{3,i} \otimes \mathbf{u}_{4,i}) \otimes (\mathbf{u}_{1,i} \otimes \mathbf{u}_{2,i}) \in \mathbb{C}^{M_S \times 1}$, where $\mathbf{u}_{r,i} = 1/\sqrt{M_r} \mathbf{T}_r^H \mathbf{a}_{N_r}(\omega_i^r) \in \mathbb{C}^{M_r \times 1}$ and can be rearranged to $\mathcal{A}_i \in \mathbb{C}^{M_3 \times M_4 \times M_1 \times M_2}$ as

$$\mathcal{A}_i = \mathbf{u}_{3,i} \times_1 \mathbf{u}_{4,i} \times_2 \mathbf{u}_{1,i} \times_3 \mathbf{u}_{2,i} \times_4 \alpha_i. \quad (17)$$

According to alternating optimization (AO) procedure [20], ω_i^r is estimated from $\mathbf{u}_{r,i}$, given fixed α_i . The mode- j unfolding of \mathcal{A}_i yields a rank-one matrix $[\mathcal{A}_i]_{(j)} = \alpha_i \mathbf{u}_{3,i} (\mathbf{u}_{4,i} \otimes \mathbf{u}_{1,i} \otimes \mathbf{u}_{2,i})^T$ and follows a cyclic pattern across different modes (i.e., $j \rightarrow r : 1 \rightarrow 3, 2 \rightarrow 4, 3 \rightarrow 1, 4 \rightarrow 2$). However, direct access to \mathbf{a}_i is unfeasible from measurements; thus, we transform \mathbf{x}_i into a four-dimensional tensor \mathcal{X}_i , mirroring the structure in (17). Upon unfolding this tensor to $[\mathcal{X}_i]_{(j)}$, we apply singular value decomposition (SVD) to estimate $\mathbf{u}_{i,r}$ by extracting the principal left-hand eigenvector $\hat{\mathbf{u}}_{i,r}$, corresponding to the highest singular value. The subsequent estimation procedures vary based on the structure of \mathbf{T}_r .

1) *Correlation-based Angle Estimation*: We start with the highest resolution dimension to estimate the angles for each detected path. The measurement vector for this spatial dimension is constructed and isolated from $[\mathcal{X}_i]_{(j)}$, and the process iterates until all path angles are resolved. Without losing generality, let $r = 3$ (corresponds to the x-axis of the

BS antenna) denote the spatial dimension with the highest resolution. The angle is then estimated by a one-dimensional search as follows.

$$\hat{\omega}_i^r = \arg \max_{\tilde{\omega}} \|\hat{\mathbf{u}}_{i,r}^H \mathbf{T}_r^H \mathbf{a}_{N_r}(\tilde{\omega})\|. \quad (18)$$

Subsequently, we decouple the contribution of ω_i^r from \mathcal{X}_i . Which for $r = 3$, this can be done by the following operation as $\mathcal{A}_i \times_1 \hat{\mathbf{u}}_{i,r}^\dagger = \epsilon_{3,i} \times_1 \mathbf{u}_{4,i} \times_2 \mathbf{u}_{1,i} \times_3 \mathbf{u}_{2,i} \times_4 \alpha_i$, where $\epsilon_{3,i} \rightarrow 1$ as $\hat{\omega}_i^r \rightarrow \omega_i^r$. Thus, we adjust the tensor \mathcal{X}_i to $\mathcal{X}_i \leftarrow \mathcal{X}_i \times_j \hat{\mathbf{u}}_{i,r}^\dagger$. This method is applied iteratively to each dimension until all angles associated with a path are estimated.

2) *ESPRIT-based Angle Estimation*: In case \mathbf{T}_r is a matrix with orthogonal columns, i.e., $\mathbf{T}_r^H \mathbf{T}_r = \mathbf{I}_{M_r}$, we implement a gridless method based on ESPRIT. In element space, the parameter ω_i^r is estimated using the shift invariance property of $\mathbf{a}_{N_r}(\cdot)$ [21]. In beamspace, this invariance is modified by \mathbf{T}_r and holds only if \mathbf{T}_r maintains a compatible structural invariance [22]. The lemma below formalizes this requirement. **Lemma 1.** Consider a unitary matrix $\mathbf{T}_r \in \mathbb{C}^{N_r \times M_r}$ where the first and last rows share an identical column span, $\mathbf{J}_1 \mathbf{T}_r = \mathbf{J}_2 \mathbf{T}_r \mathbf{\Gamma}$, where $\mathbf{J}_1 = [\mathbf{I}_{N_r-1} \ \mathbf{0}_{N_r}]$, $\mathbf{J}_2 = [\mathbf{0}_{N_r} \ \mathbf{I}_{N_r-1}]$, and $\mathbf{\Gamma} \in \mathbb{C}^{M_r \times M_r}$ is nonsingular. Defining $\mathbf{T}_r^H = [\mathbf{t}_1, \mathbf{t}_2, \dots, \mathbf{t}_{N_r}]$, if a matrix $\mathbf{\Phi} \in \mathbb{C}^{M_r \times M_r}$ satisfies $\mathbf{\Phi} \mathbf{t}_{N_r} = \mathbf{0}$ and $\mathbf{\Phi} \mathbf{\Gamma}^H \mathbf{t}_1 = \mathbf{0}$, then

$$\mathbf{\Phi} \hat{\mathbf{u}}_{r,i} = \mathbf{\Phi} \mathbf{\Gamma}^H \hat{\mathbf{u}}_{r,i} \exp(j\omega_i^r). \quad (19)$$

Proof. See [22]. \square

The matrix $\mathbf{\Phi}$ orthogonally projects vectors onto the null space of \mathbf{t}_{N_r} and $\mathbf{\Gamma}^H \mathbf{t}_1$. To compute $\mathbf{\Phi}$, construct \mathbf{P} by aligning these vectors as columns, then derive

$$\mathbf{\Phi} = \mathbf{I}_{M_r} - \mathbf{P}(\mathbf{P}^H \mathbf{P})^{-1} \mathbf{P}^H. \quad (20)$$

Using (19) and (20), an estimate for ω_i^r is given by

$$\hat{\omega}_i^r = \arg \left((\mathbf{\Phi} \mathbf{\Gamma}^H \hat{\mathbf{u}}_{r,i})^\dagger \mathbf{\Phi} \hat{\mathbf{u}}_{r,i} \right). \quad (21)$$

E. Modification for Non-resolvable Paths in Delay Domain

The method's effectiveness relies on resolving paths in the delay domain, which generally provides the highest resolution. However, closely spaced paths in delay that are separable in spatial domains remain undetected. Consider \bar{L} paths that share identical delay values, resulting in a single delay estimate $\hat{\tau}_i$. After delay mitigation, (17) modifies to $\mathcal{A}_i = \mathbf{u}_{3,i} \times_1 \mathbf{u}_{4,i} \times_2 \mathbf{u}_{1,i} \times_3 \mathbf{u}_{2,i} \times_4 \bar{\alpha}$, where $\bar{\alpha} = [\alpha_{i,0} \ \alpha_{i,1} \ \dots \ \alpha_{i,\bar{L}-1}]$. Instead of estimating the path with the largest $\alpha_{i,\bar{l}}$, the maximization in (18) is modified to detect \bar{L} paths (i.e., $\hat{\omega}_{i,\bar{l}}^r$ for $\bar{l} \in \{0, 1, \dots, \bar{L} - 1\}$) by a one-dimensional search over $\|\hat{\mathbf{u}}_{i,r}^H \mathbf{T}_r^H \mathbf{a}_{N_r}(\tilde{\omega})\|^2$ followed by a CA-CFAR detector with automatic threshold [18]. Further, we construct $\bar{\mathbf{U}}_{i,r} = [\tilde{\mathbf{u}}_{i,0,r} \ \tilde{\mathbf{u}}_{i,1,r} \ \dots \ \tilde{\mathbf{u}}_{i,\bar{L},r}]$. Mirroring Section III-C, the dimension r is decoupled as

$$\mathcal{A}_i \times_j \bar{\mathbf{U}}_{i,r}^\dagger = \mathcal{A}_{\text{sub},i,0} \sqcup \mathcal{A}_{\text{sub},i,1} \sqcup \dots \sqcup \mathcal{A}_{\text{sub},i,\bar{L}-1}, \quad (22)$$

where for $r = 3$, $\mathcal{A}_{\text{sub},i,\bar{l}} = \epsilon_{3,i} \times_1 \mathbf{u}_{4,i} \times_2 \mathbf{u}_{1,i} \times_3 \mathbf{u}_{2,i} \times_4 \alpha_{i,\bar{l}}$. Following Section III-D1 and (22), the input for the next dimension is $\mathcal{X}_{i,\bar{L}+\bar{l}} \leftarrow \mathcal{X}_{\text{sub},i}^{l,i,i,i}$, where $\mathcal{X}_{\text{sub},i} = \mathcal{X}_i \times_j \bar{\mathbf{U}}_{i,r}^\dagger$.

²Alternatively, the ESPRIT-type approach could be employed to estimate these angles instead of searching for peaks. However, ESPRIT requires an additional structural constraint and prior knowledge of the number of paths in the spatial domain, which is why it was not adopted here.

¹For now, we assume all paths have distinct delays; the special case where paths have identical delays is addressed in Section II-E.

IV. RESULTS

A. Simulation Setup

We simulate a downlink scenario with one LoS and one non-line-of-sight (NLoS) component, with angular frequencies

$$\Omega = \begin{bmatrix} \omega_0 \\ \omega_1 \end{bmatrix}^T = \begin{bmatrix} -1.08 & -0.31 & 0.38 & 0.21 & -0.20 \\ -0.03 & 0.16 & 0.61 & -0.46 & -0.21 \end{bmatrix}^T.$$

where ranges are calculated as $-397.61 \times \omega_r^5 = [80 \ 85]$ meters. In default, the BS has $N_{BS} = N_1 \times N_2 = 16 \times 24$ antennas, while the UE has $N_{UE} = N_3 \times N_4 = 4 \times 16$ antennas, both spaced at half the wavelength $\lambda/2$. The system operates at 27.2 GHz with a bandwidth of 3300×120 kHz. The OFDM frame includes $S = M_1 \times M_2 = 4 \times 34$ symbols per block and $M = M_3 \times M_4 = 4 \times 8$ symbols per user beam, and $p_{FA} = 10^{-6}$. The noise PSD is -174 dBm/Hz, and the noise figure is 10 dB. Experiments evaluate accuracy, resolution, and complexity, comparing the proposed with SoTA estimators.

The proposed methods include FFT-CB (correlation-based angle estimation), FFT-CB (Modified) (handling non-resolvable paths), and FFT-ESPRIT (ESPRIT-based angle estimation). Comparisons are made with RDB-ESPRIT [4], SVD-CB [23], and the maximum likelihood estimator (MLE). Unlike methods compared, the proposed approaches do not require prior path count knowledge. Moreover, FFT-CBs, SVD-CB, and MLE utilize all 34 beams without precoder orthogonality, while subspace methods use 24 orthogonal beams out of 34 beams.

B. Evaluation Metrics

The root mean squared error is not used as it lacks auto-pairing information and does not account for missed detections or false alarms. In our performance evaluation, we use the generalized optimal sub-pattern assignment (GOSPA) [24], with exponent value 1, cut-off distance $2\pi/\min([N_1, N_2, N_3, N_4, K])$, and the cardinality penalty 2. To evaluate complexity, we measure computation time per iteration on a system with a 13th Gen Core-i7 CPU and 32 GB RAM. The shown results are averages over 250 Monte Carlo simulations per data point.

C. Simulation Scenarios

1) *Accuracy*: Fig. 1 compares the GOSPA across estimators versus transmit power. The proposed FFT-based methods achieve the SNR threshold at lower power than subspace approaches due to inherent DFT gain. Accuracy improves until 30 dBm for FFT-CB and FFT-CB (Modified), and 16 dBm for FFT-ESPRIT, but they approach a plateau because the estimation based on DFT bin limits the delay accuracy. Note FFT-ESPRIT is not as performant as it uses only 24 of 34 beams. The SVD-based method requires higher power to reach its SNR threshold but continues to improve with power (no plateau observed). RDB-ESPRIT performs worst, as its tensor decomposition demands a high SNR per beam/subcarrier to converge.

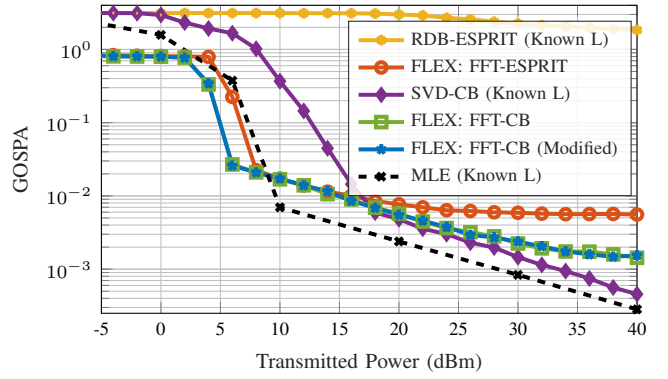


Fig. 1. GOSPA of the selected estimators versus the transmitted power.

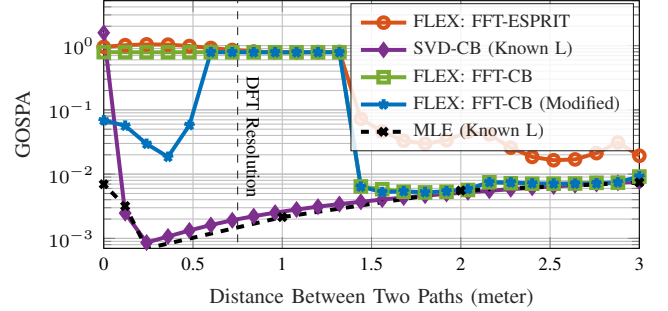


Fig. 2. GOSPA of the estimators versus range difference between two paths.

2) *Resolution*: Fig. 2 shows each estimator's ability to separate two close-range paths with 45 dBm transmitted power for the UE. The first path remains fixed at 80 m, while the second moves closer from 83 m to 80 m. As expected, SVD-CB, a super-resolution method, closely follows MLE. The resolution of FFT-CB and FFT-ESPRIT is constrained to approximately twice the DFT resolution, which is ~ 0.75 m. This limitation occurs as the detector requires two consecutive windows to extract peaks.

The proposed FFT-CB (Modified) mitigates this limit, detecting both paths from 0 m to 0.5 m separation. However, between 0.6 m and 1.4 m, it detects only one path. Fig. 3 clarifies this behavior with periodograms and beam-correlation profiles. At 0.25 m separation, the periodogram shows a single peak, yet FFT-CB (Modified) detects the secondary beam correlation peak corresponding to the second path. At 0.75 m, the second path is obscured by the sidelobe of the first, so its peak is not detected. This occurs because the delay bin under analysis is sufficiently distant from the true delay of the second path, causing its energy to be filtered out during the delay mitigation stage, leaving only a single detectable peak in the AoD dimensions.

3) *Complexity*: Fig. 4 illustrates the computational overhead as subcarriers increase. Although SVD-CB achieves high accuracy, it exceeds 16 sec per iteration, making it suitable for offline applications. The proposed FFT-based methods remain under 1 sec, outperforming even RDB-ESPRIT, which is typically considered low-complexity. Among the FFT approaches, FFT-ESPRIT is the fastest, due to its gridless estimation.

Fig. 5 breaks down computation time for each method. For SVD-CB and RDB, the dominant costs, SVD and CP

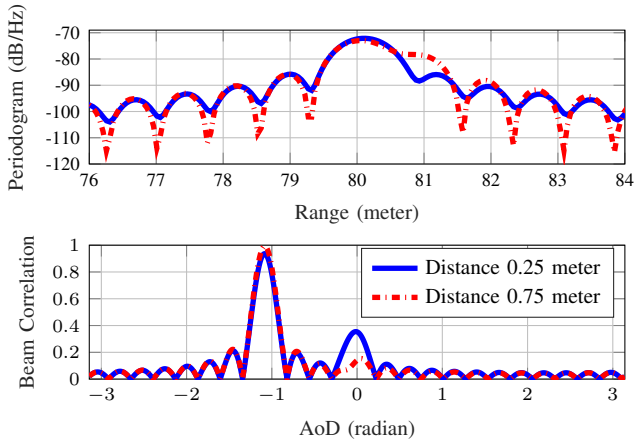


Fig. 3. Periodogram (top) and beam-correlation (bottom) profiles illustrating how Modified FFT-CB resolves two close paths.

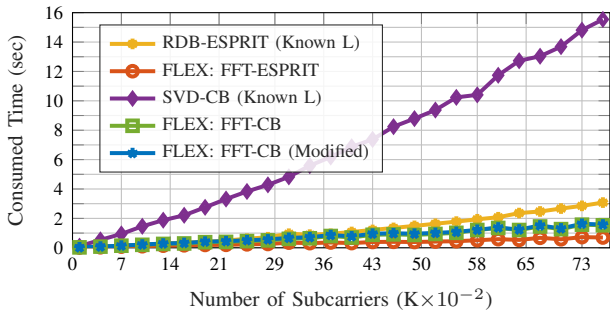


Fig. 4. Computation time of each estimator versus the number of subcarriers.

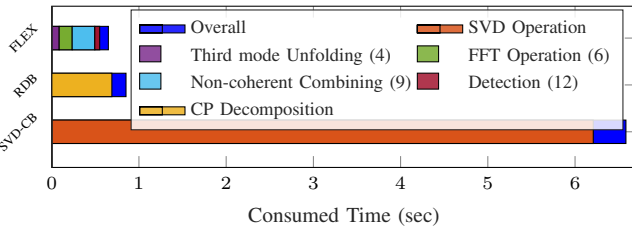


Fig. 5. Breakdown of computational time for each estimator at default settings.

decomposition, are already highly optimized in MATLAB. In contrast, FLEX : FFT-CB is mainly affected by FFT (6), and non-coherent combining (9). This suggests that selecting fewer relevant columns instead of combining all could potentially decrease complexity even further.

V. CONCLUSION

We proposed FLEX, a family of low-complexity FFT-based beamspace channel estimators for mmWave MIMO-OFDM. These methods estimate propagation delays via an FFT-based periodogram with CA-CFAR detection, then eliminate delays to decouple spatial dimensions. Angle estimation is performed using CB or ESPRIT, with a modified CB method resolving non-resolvable paths in the delay domain. Simulations show that FLEX achieves competitive accuracy with SoTA methods at significantly lower computational cost while automatically pairing the parameters and estimating the number of paths. Future work includes extending FLEX to ultra-wideband channels by addressing frequency-selective effects and evaluating its performance on real-world measurements.

REFERENCES

- [1] R. W. Heath. *et al.*, “An overview of signal processing techniques for millimeter wave MIMO systems,” *IEEE Journal of Selected Topics in Signal Processing*, vol. 10, no. 3, pp. 436–453, 2016.
- [2] J. Lee *et al.*, “Channel estimation via orthogonal matching pursuit for hybrid MIMO systems in millimeter wave communications,” *IEEE Transactions on Communications*, vol. 64, no. 6, pp. 2370–2386, 2016.
- [3] X. Wei and L. Dai, “Channel estimation for extremely large-scale massive MIMO: Far-field, near-field, or hybrid-field?” *IEEE Communications Letters*, vol. 26, no. 1, pp. 177–181, 2022.
- [4] F. Wen *et al.*, “Tensor decomposition based beamspace ESPRIT for millimeter wave MIMO channel estimation,” in *2018 IEEE Global Communications Conference (GLOBECOM)*. Abu Dhabi, UAE: IEEE, 2018, pp. 1–7.
- [5] F. Jiang *et al.*, “High-dimensional channel estimation for simultaneous localization and communications,” in *IEEE Wireless Communications and Networking Conference (WCNC)*, Nanjing, China, 2021, pp. 1–6.
- [6] Z. Lin *et al.*, “Tensor-based multi-dimensional wideband channel estimation for mmwave hybrid cylindrical arrays,” *IEEE Transactions on Communications*, vol. 68, no. 12, pp. 7608–7622, 2020.
- [7] T. S. Rappaport *et al.*, “Wideband millimeter-wave propagation measurements and channel models for future wireless communication system design,” *IEEE Transactions on Communications*, vol. 63, no. 9, pp. 3029–3056, 2015.
- [8] O. El Ayach *et al.*, “Spatially sparse precoding in millimeter wave MIMO systems,” *IEEE Transactions on Wireless Communications*, vol. 13, no. 3, pp. 1499–1513, 2014.
- [9] A. Alkhateeb *et al.*, “Channel estimation and hybrid precoding for millimeter wave cellular systems,” *IEEE journal of selected topics in signal processing*, vol. 8, no. 5, pp. 831–846, 2014.
- [10] Y. Lin *et al.*, “Tensor-based channel estimation for millimeter wave MIMO-OFDM with dual-wideband effects,” *IEEE Transactions on Communications*, vol. 68, no. 7, pp. 4218–4232, 2020.
- [11] R. Zhang *et al.*, “Tensor decomposition-based channel estimation for hybrid mmwave massive MIMO in high-mobility scenarios,” *IEEE Transactions on Communications*, vol. 70, no. 9, pp. 6325–6340, 2022.
- [12] L. Cheng *et al.*, “Probabilistic tensor canonical polyadic decomposition with orthogonal factors,” *IEEE Transactions on Signal Processing*, vol. 65, no. 3, pp. 663–676, 2016.
- [13] J. Wang *et al.*, “Beam codebook based beamforming protocol for multi-gbps millimeter-wave wpan systems,” *IEEE Journal on Selected Areas in Communications*, vol. 27, no. 8, pp. 1390–1399, 2009.
- [14] J. Hong *et al.*, “A tensor-based millimeter wave wideband massive MIMO channel estimation technique using uniform planar arrays,” *IEEE Wireless Communications Letters*, 2024.
- [15] T. G. Kolda, “Multilinear operators for higher-order decompositions,” Sandia National Laboratories (SNL), Albuquerque, NM, and Livermore, CA, Tech. Rep., 2006.
- [16] W. Sun and H.-C. So, “Accurate and computationally efficient tensor-based subspace approach for multidimensional harmonic retrieval,” *IEEE Transactions on Signal Processing*, vol. 60, no. 10, pp. 5077–5088, 2012.
- [17] M. H. Hayes, *Statistical Digital Signal Processing and Modeling*. John Wiley & Sons, 1996, ch. 8.2.4, p. 412.
- [18] M. A. Richards *et al.*, *Fundamentals of radar signal processing*. Mcgraw-hill New York, 2005, vol. 1.
- [19] D. R. Fuhrmann *et al.*, “A cfar adaptive matched filter detector,” *IEEE Trans. Aerosp. Electron. Syst.*, vol. 28, no. 1, pp. 208–216, 1992.
- [20] J. C. Bezdek and R. J. Hathaway, “Some notes on alternating optimization,” in *Advances in Soft Computing—AFSS 2002: 2002 AFSS International Conference on Fuzzy Systems Calcutta, India, February 3–6, 2002 Proceedings*. Springer, 2002, pp. 288–300.
- [21] R. Roy and T. Kailath, “ESPRIT-estimation of signal parameters via rotational invariance techniques,” *IEEE Transactions on acoustics, speech, and signal processing*, vol. 37, no. 7, pp. 984–995, 1989.
- [22] G. Xu *et al.*, “Beamspace ESPRIT,” *IEEE Transactions on Signal Processing*, vol. 42, no. 2, pp. 349–356, 1994.
- [23] J. Hong *et al.*, “A tensor-based millimeter wave wideband massive MIMO channel estimation technique using uniform planar arrays,” *IEEE Wireless Communications Letters*, 2024.
- [24] A. S. Rahmathullah *et al.*, “Generalized optimal sub-pattern assignment metric,” in *2017 20th International Conference on Information Fusion (Fusion)*. Xi’an, China: IEEE, 2017, pp. 1–8.